

Magnetism of metastable γ -Fe₈₅Pd₁₅ nanowire arrays across an unusually broad temperature range (5 K to 800 K)

Paula G. Bercoff^{1,2,*}, Soledad Aprea^{1,2}, Eva Céspedes³,
José Luis Martínez³, Silvia E. Urreta¹, Manuel Vázquez³

¹ Universidad Nacional de Córdoba. Facultad de Matemática, Astronomía, Física y Computación (FAMAF). Ciudad Universitaria, 5000 Córdoba, Argentina.

² CONICET, Instituto de Física Enrique Gaviola (IFEG). Ciudad Universitaria, 5000 Córdoba, Argentina.

³Instituto de Ciencia de Materiales de Madrid, CSIC. E-28049 Madrid, Spain.

Abstract (245 words)

Arrays of 50 nm diameter Fe₈₅Pd₁₅ cylindrical nanowires were electrochemically grown, crystallizing in a metastable γ -Fe(Pd) *fcc* A1 disordered solid solution. After performing a heating-cooling thermal cycle between 300K and 1000K, the γ -Fe(Pd) *fcc* metastable phase still predominates (97%), coexisting with a not-fully-identified minority phase. The thermal cycling induces a moderate increase in the crystallite size and a reduction of the lattice parameter although leading to a significant heating-cooling magnetic hysteresis. No further changes in temperature-dependent magnetization, $M(T)$, are observed during subsequent cycling. The full-range (5K to 800K) saturation magnetization $M_s(T)$ curve is quite accurately described by a phenomenological expression, which provides a Bloch-type contribution as $T \rightarrow 0$ and undergoes the critical behavior $M(T) \approx (T_c - T)^{\frac{1}{\beta}}$ near the Curie temperature T_c . An upturn in $M_s(T)$ is observed below 100 K which is described by a spin-glass-like second contribution, with freezing temperature $T_f = (80 \pm 2)$ K, and $k_B T_f$ comparable to the exchange interactions in Fe-Pd systems. A Curie temperature of $T_c = 830$ K, and a critical exponent value $\beta = 0.42 \pm 0.05$ are estimated. These regimes (below and above 100K) are also observed in the magnetization process. The temperature dependence of coercivity between 100K and 800K is consistent with a nucleation/propagation remagnetization mechanism, with activation energy of (320 ± 20) kJ mol⁻¹ and critical field for magnetization reversal of (65 ± 1) mT, at 0K. The analysis of the effective magnetic anisotropy as a function of temperature allows us to conclude that it essentially arises from the balance between different magnetostatic contributions.

Keywords: Fe-Pd nanowire arrays; electrodeposition; Fe-rich Fe-Pd alloy; γ -Fe(Pd) phase; effective magnetic anisotropy; hysteresis properties.

1. Introduction

Fe-Pd alloys are transition/noble-metal bimetallic systems with interesting properties and applications. For different compositions, they exhibit invar properties [1-3], magnetostriction [4], magnetic anisotropy high enough for perpendicular magnetic recording [5], or ferromagnetic shape memory (FSM) [6]. In addition to FSM [7-10], higher ductility and better corrosion resistance in comparison to the “prototype” FSM alloy Ni-Mn-Ga has been proved. Besides the heat resistant properties at elevated temperatures, an excellent biocompatibility [11] has been demonstrated in Fe-Pd thin films, making the Fe-Pd alloys a promising alternative in many applications.

In the last decades, low-dimensional nanostructures based on this alloy series have been intensively investigated, such as nanoparticles [12] or Fe-Pd 1D (nanowires) [13-15] and 2D (thin films) [16, 17] with

different compositions produced by electrodeposition, a relatively low-cost and practical technique.

The bimetallic Fe-Pd system has a quite rich structural phase diagram [18]; at high temperatures, below the solidus line, a thermodynamically stable disordered γ -Fe_xPd_{100-x} *fcc* type solid solution exists in the whole composition range. However, in the intermediate- and low- T regimes the Fe-Pd system becomes more complex, with many different stable and even metastable phases which are strongly dependent on the alloy composition as well as on the previous heat-treatment history details.

At room temperature, for iron concentration $x \geq 70$, α -Fe_xPd_{100-x} alloys with a *bcc*-type structure are found, while for $x \leq 60$ phases with *fcc*-type lattice are observed [19, 20]. The high temperature disordered γ -Fe_xPd_{100-x} alloys having compositions around $x = 50$ at. % Fe and 25 at. % Fe undergo a disorder-order transformation on cooling. Alloys with $40 \leq x \leq 50$, order to L1₀ type superstructure via a thermodynamically order-disorder transformation of

first order, to achieve a tetragonal structure, by alternating stacking of Fe and Pd planes along the [001] principal axis with respect to the *fcc*-lattice. In the composition range $14 \leq x \leq 38$, the ordered phase is the cubic FePd₃ phase, with L1₂-type structure. Atomic rearrangements at low *T* are often hindered by the sluggish kinetics of the equilibrium approach, leading to metastability. In these cases, slow diffusion processes limit the reaction pathway making difficult the transformation to more stable structures.

Fe–Pd low dimensional nanostructures synthesized by electrodeposition near room temperature are found to consist of a disordered, metastable γ -Fe_{*x*}Pd_{100-*x*} phase in all the composition range, as also found in bulk samples quenched from high temperature, where solubility is complete. The as-deposited nanostructures are then heat-treated at temperatures above 830 K to promote the stable phase separation corresponding to the given composition. As soon as atomic mobility is enabled via a vacancy-mediated atomic diffusion process during heating, two simultaneous processes begin: defect recovery and long-range ordering.

While most of the investigations to date have been performed within an intermediate range of compositions in the Fe-Pd system, little has been reported about the hysteresis and structural transformations in high Fe content Fe-Pd alloys, and specifically on metastable Fe-rich γ -Fe_{*x*}Pd_{100-*x*} alloys.

In this article, we report for the first time that the *fcc* disordered metastable γ -Fe₈₅Pd₁₅ phase initially observed in as-electrodeposited nanowires (NWs) remains almost unchanged, without transforming to the expected equilibrium *bcc* α -phase nor undergoing ordering, even after thermal cycling between 350 K and 800 K. This interesting fact has allowed us to completely characterize the magnetic properties of this disordered solid solution in a quite broad temperature range, describing the main magnetization mechanism, the effective anisotropy controlling coercivity and also the critical exponent associated to the ferro-paramagnetic transition. In addition to these fundamental physical properties, a spin-glass-like contribution to overall magnetization is detected below 100 K, associated to the NW's large area/volume ratio. The large resilience of this phase to structural (phase) transformations is crucial for applications where the material is exposed to high temperatures for extended periods. As this *fcc* phase also retains good mechanical properties and oxidation resistance, it is also suitable for small components operating under high thermal stress.

2. Experimental

2.1. Nanoporous alumina membranes

High-purity aluminum foils (Al 99.997%, Alfa Aesar) were used to synthesize anodized aluminum oxide (AAO) templates with hexagonally self-assembled cylindrical nanopores through conventional two-step anodization [21]. Before anodizing, the aluminum foils were degreased with acetone and electropolished in an ethanol: perchloric acid 3:1 v/v solution. Then, the foils were anodized under a constant voltage of 40 V in 0.3 M H₂C₂O₃ for 24 h at 276 K to form an alumina layer of disordered pores. After the first anodizing step, the alumina film was removed by dissolving in a 0.20 M Cr₂O₃ and 0.40 M H₃PO₄ solution for 36 h. Then, a second anodizing step was carried out under the same conditions as the first one, for another 24 h. Before using as templates for NW electrodeposition, the AAO membranes were immersed in a 5% v/v H₃PO₄ solution for a few minutes to widen the pores and reduce the barrier layer.

The porous alumina membranes used as templates were imaged by scanning electron microscopy, SEM (not shown), to estimate the pore diameter *D*, the center-to-center interpore distance *d*_{cc} histograms, and the porosity *P* ($= \pi/2\sqrt{3}(D/d_{cc})^2$) [22]. The templates exhibit self-assembled pores in a hexagonal lattice with *D* = (50±2) nm; *d*_{cc} = (110±5) nm and *P* = (0.20±0.05).

2.2. Electrodeposition of Fe-Pd NWs

Fe-Pd nanowires were electro-synthesized using the above-described AAO membranes as templates and electrolytic baths with FeCl₃ and PdCl₂ salts in ultrapure water. The supporting electrolyte was ammonium citrate 0.3M, and ammonium hydroxide 0.25 M was added to the solution in order to keep the pH = 9.00. The NWs composition was controlled by selecting the Fe³⁺ and Pd²⁺ ions concentration in the electrolytic bath. Fe₈₅Pd₁₅ NWs were obtained using an electrolytic bath of 75/10 mM iron/palladium ratio and alumina (AAO) templates obtained as described in Section 2.1. Prior to use, a conductive thin gold layer was deposited by sputtering on one side of the AAO membrane, in order to be used as cathode. Electrodeposition was carried out at 40°C in order to promote the formation of ordered phases [15] using a potentiostat/galvanostat Autolab and a three-electrode cell: a commercial Ag/AgCl electrode was used as a reference and a Pt wire as a counter electrode. The electrodeposition potential was -1.1 V vs. Ag/AgCl, during a deposition time of 30 min. These conditions produced 1.4 μm long NWs. The obtained sample is denoted by the iron at.% composition, that is, Fe85= Fe₈₅Pd₁₅. The mean composition of the arrays was determined by SEM-EDS after measuring many

relatively large zones in the sample to improve the statistical error, which in all cases was ± 2 at. %.

2.3 Characterization

The morphology and composition of the NWs were determined with a Sigma Zeiss scanning electron microscope (SEM) and an Oxford detector, respectively. NWs' lengths and diameters were measured directly from SEM images covering large areas of the arrays: the corresponding histograms were built up with these data and mean values and standard deviations were then estimated by fitting a normal profile to the distributions. X-ray diffractograms (XRD) were measured in a Bruker D8 Advance diffractometer at 40 kV and 30 mA, using Cu K_{α} radiation ($\lambda = 1.5418 \text{ \AA}$) in Bragg-Brentano configuration. The crystallite size s in the as-deposited state and after the thermal cycle were estimated using the Williamson-Hall relationship: $\ln \beta_w = \ln \frac{\kappa \lambda}{s} + \ln \frac{1}{\cos \theta}$, with $\kappa = 0.9$ (spherical crystallites are assumed), $\lambda = 1.5418 \text{ \AA}$, θ the Bragg angles and β_w the FWHM (Full Width at Half Maximum) of the *fcc* γ -Fe(Pd) peaks, after correction for instrumental broadening. Strains in the samples were neglected, so only the contribution of crystallite size to peak widening was considered.

Microstructural details were determined by TEM-STEM techniques in a TEM TALOS F200X device, equipped with 4 windowless SDD Super-X detector system. For TEM characterization, the alumina template was dissolved in chromic acid during a few days, and the released nanowires were washed several times in ethanol. Then, a drop of the solution was deposited on a carbon-coated copper grid.

The low-temperature magnetic properties were measured in a Cryogenic vibrating sample magnetometer (VSM) from 5 K to 350 K. A SQUID magnetometer (MPMS-3), from Quantum Design (San Diego, USA), supplying a maximum magnetic field of 7 T and a furnace option allowing sensitive magnetic measurements at controlled high temperatures, was used to measure the magnetic properties between 300 K and 1000 K. A special ceramic holder was utilized to measure between 300 and 1000 K and a special alumina cement was used to fix the samples to the holder, before covering the ensemble with a non-magnetic Cu foil. Hysteresis loops were measured with the magnetic field applied both parallel (PA) and perpendicular (PE) to the NW's axis. All the magnetic measurements were performed while keeping the NWs within the template.

3. Results and discussion

3.1. Morphology and Microstructure

A SEM image of the NWs after partial dissolution of the alumina template is displayed in Figure 1, together with histograms of the NWs diameter and length obtained from measuring several images in order to have good statistics. The NWs replicate the pores cylindrical shape with a quite constant diameter $d = (50 \pm 5) \text{ nm}$, and length $L = (1.4 \pm 0.2) \mu\text{m}$, resulting in a large aspect ratio ($A_R = L/d = 30 \pm 5$).

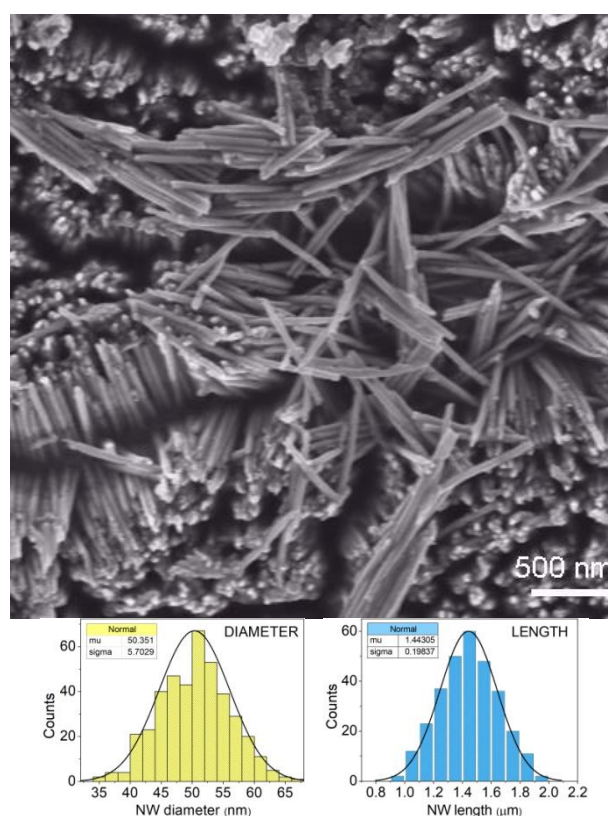


Figure 1. SEM image corresponding to Fe85 NWs, after being partially released from the alumina template. Histograms of the NWs diameter and length were obtained by measuring several images.

Figure 2 displays (upper panel) the room temperature X-ray diffractogram corresponding to the as-deposited Fe85 nanowire array. Measurements were performed with the X-ray beam incident on the array's bottom surface, after removing most of the gold layer. In the as-deposited sample, peaks corresponding to a majority (97%) γ -Fe(Pd) *fcc* disordered (A1) phase and to the α -Fe₃Pd *bcc* solid solution phase are indexed, together with extra peaks arising from the remnant of the sputtered gold.

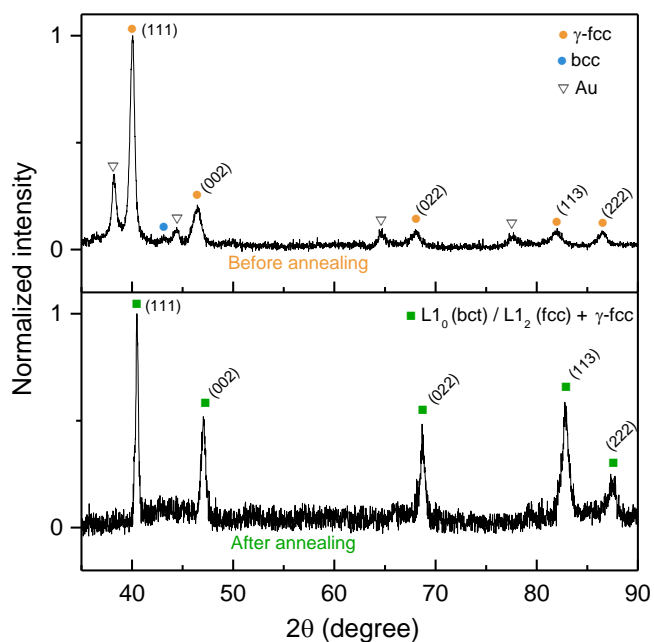


Figure 2. X-ray diffractograms of Fe₈₅ in the as-deposited state (before annealing, upper pattern) and after a heating-cooling thermal cycle, between 350 K and 1000 K at 10 K/min (lower pattern).

The crystallographic phases and grain substructure in the as-deposited NWs were further characterized with TEM and STEM and the results are summarized in Figure 3. Composition values and Fe/Pd maps obtained from HAADF imaging are depicted in Figure 3a and Figure 3b for an individual NW, confirming that these elements are alloyed with a composition of about 85 at. % Fe, close to that obtained with SEM-EDS. TEM (Figure 3c) and HRTEM (Figure 3d) images confirm that the nanowires are polycrystalline, with mean grain size of about 16 nm, a value which is statistically indistinguishable from that estimated for the mean value of crystallite size with XRD data and the Williamson-Hall formula ($s = (15 \pm 5)$ nm). The electron diffraction pattern (FFT from the indicated zone) shown in the inset of Figure 3d is consistent with a *fcc* lattice, as observed in the X-ray data.

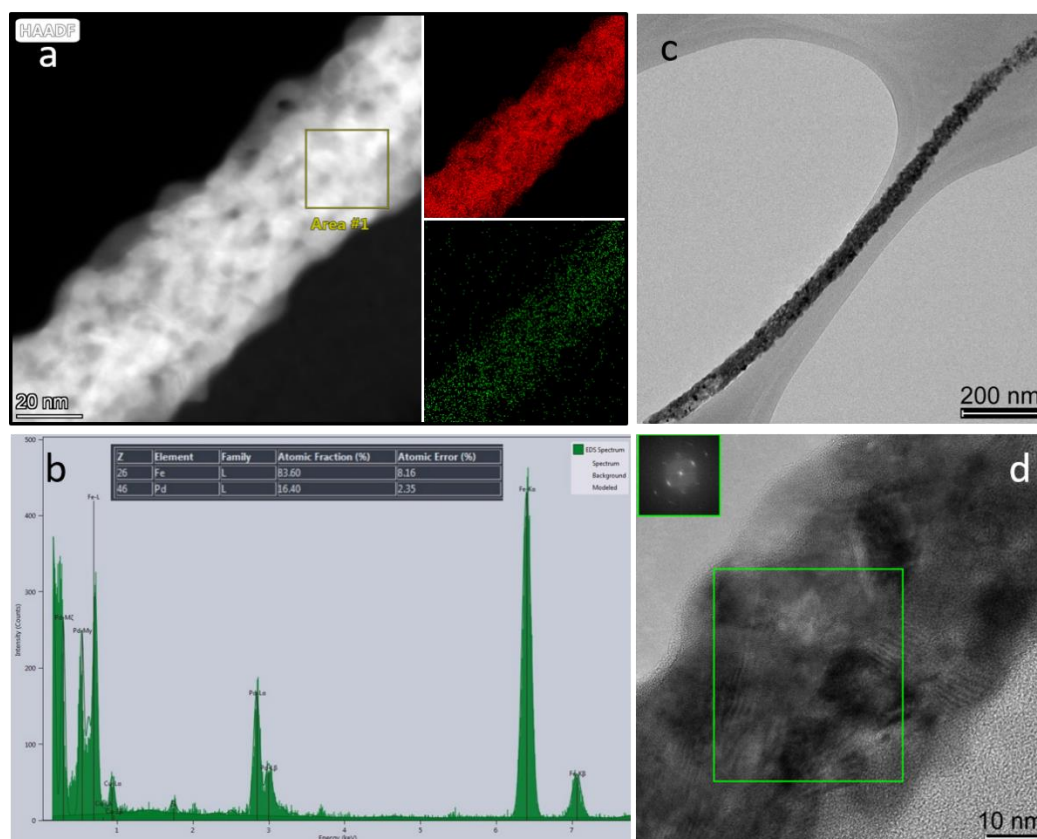


Figure 3. a) HAADF image with the corresponding composition maps for Fe (up) and Pd (down), indicating that these elements are alloyed. b) X ray emission spectrum from the marked zone in (a). c) Bright field TEM image of a single polycrystalline NW, with a diameter consistent with the value of (50 ± 5) nm determined by SEM. d) HRTEM image of a NW showing small grains of 15 nm mean size. Inset: FFT of the squared zone, confirming a *fcc* phase.

These metastable atomic phases are expected to remain unchanged during measuring the magnetic properties at low temperature, while above room temperature (up to 1000 K), phase and/or ordering transformations can be promoted in addition to magnetic phase transitions, leading to complex effects during thermal cycling. Then, before measuring the magnetic hysteresis properties above room temperature, a thermal treatment consisting in a heating-cooling thermal cycle between 350 K and 1000 K, at 10 K/min was performed, which proved to be enough to reach a stable atomic microstructure during further high temperature measurements.

The XRD pattern corresponding to the final microstructure after the thermal cycle annealing is shown in the lower panel of Figure 2. A similar volume fraction of the original γ -Fe(Pd) *fcc* disordered phase is still detected together with a quite small fraction ($\sim 3\%$) of an ordered *fcc* phase, replacing the original α phase, which may be the $L1_0$ FePd equiatomic phase or the $L1_2$ Fe₃Pd iron-rich one. As the majority phase peaks shift to higher angles after the thermal cycle ($\Delta\theta \sim 0.2^\circ$), they overlap with the peaks of the minority phase, making it difficult to perform a confident identification of this secondary phase. Summarizing, from the data in Figure 2 and Figure 3, the crystallite size of the γ -Fe(Pd) phase is (15 ± 5) nm in the as-deposited state and (27 ± 5) nm after the thermal treatment, while the crystallite size of the minority phase is ~ 9 nm in both conditions. The reduction in the lattice constant of the γ -Fe(Pd) phase observed after the high temperature cycle (from $a = 3.8980$ Å before the thermal cycle to $a = 3.8873$ Å afterwards) indicates that some atomic rearrangements take place, likely leading to a more relaxed structure and a more uniform matrix composition, but not large enough to achieve a phase transition to the equilibrium phases.

The changes in atomic structure and magnetic configurations during the thermal cycle were explored by measuring the evolution of the as-deposited array magnetization during a thermal cycle between 350 K to 1000 K, at a constant rate of 10 K/min. The temperature dependence of the NW array magnetic moment was measured under an external magnetic field of 100 mT (about 1/10 of the saturation field), applied parallel (PA orientation) to the NW's axis. The obtained curves—shown in Figure 4—display heating-cooling hysteresis indicating that some changes in the initial crystalline phases take place.

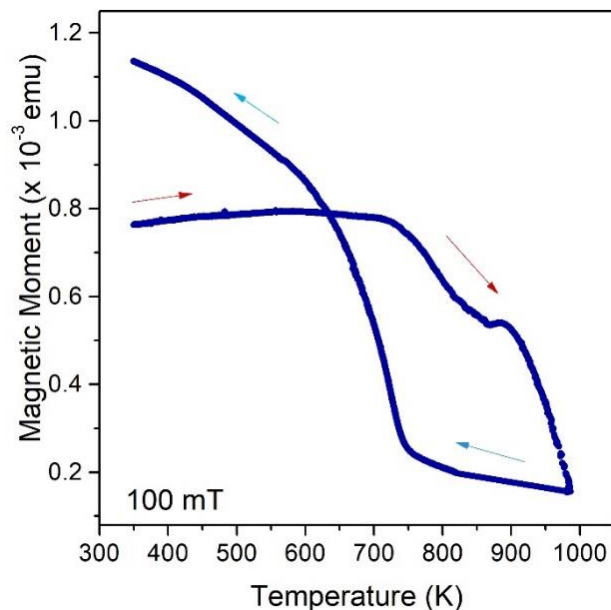


Figure 4. Magnetic moment of the as-deposited array during the first thermal cycle between 350 K to 1000 K, at a constant rate of 10 K/min, measured under an external magnetic field of 100 mT, applied parallel (PA orientation) to the NW's axis. The red arrows pointing right indicate the heating and the blue arrows pointing left indicate cooling measurements.

The initial heating curve in Figure 4 (indicated with red arrows) exhibits nearly constant magnetization values up to about 750 K (increasing only by 1.8%); then, it notably decreases displaying a marked shoulder above 830 K, a temperature quite close to 823 K, reported for the ordering debut in these metastable γ -Fe(Pd) alloys [23]. This indicates that above this temperature, magnetic and atomic processes overlap in the measured magnetization. After cooling and completing the thermal cycle, the magnetization is higher than at the beginning, confirming that some atomic rearrangements took place in the microstructure. All the magnetic measurements above room temperature were performed after a thermal cycle as the one just described.

These diffusion-controlled rearrangements in the γ -Fe(Pd) matrix at high temperature (which are also detected by XRD measurements) are responsible for the heating-cooling hysteresis observed in Figure 4. It may be then concluded that the annealing tends to stabilize the initial main phase and changes the precipitated phase, leading to a microstructure that remains unchanged during subsequent thermal cycles below 1000 K. Then, magnetic measurements performed in the as-deposited condition at low temperature (below

room temperature) should be well correlated to those performed at temperatures above 300 K and up to 1000 K, because the initial atomic microstructure in the as-deposited array is quite similar to that obtained after the high temperature thermal treatment. The changes underwent by the small precipitates are not detected, likely because of their small volume fraction in both conditions.

In what follows, the magnetic hysteresis properties at low temperature (below 400 K) are first characterized and then the same magnetic properties are measured at high temperature in the thermally treated array. Finally, hysteresis properties are analyzed in the whole temperature range.

3.2. Magnetic hysteresis properties

The activation energy barrier distributions, associated with the magnetization mechanisms at low temperature, were characterized by measuring M vs. T curves following the zero field cooling-field cooling (ZFC-FC) protocol between room temperature and 5 K, under a constant applied field of 40 mT.

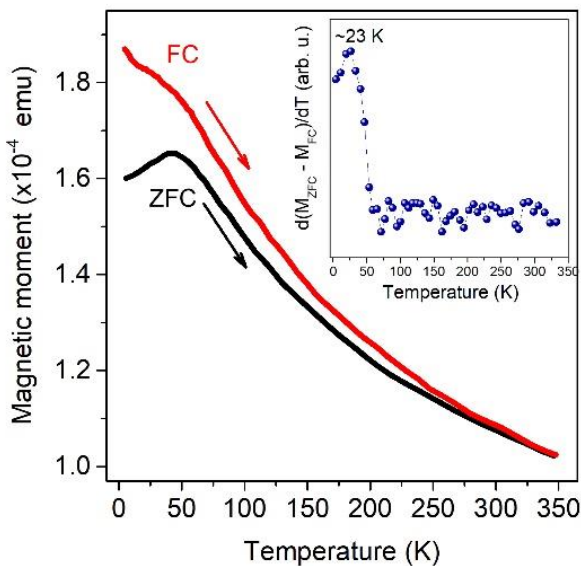


Figure 5. Magnetization vs. temperature curves obtained following the ZFC-FC protocol in the as-deposited condition, measured under an applied field of 40 mT, at 10 K/min. Arrows indicate that measurements were performed on heating. The inset shows the temperature dependence of the $\frac{d(M_{FC}-M_{ZFC})}{dT}$ derivative.

ZFC and FC curves overlap above the irreversibility temperature $T_{irr} \cong 350$ K, and a local maximum is observed near 30 K; these results are depicted in [Figure 5](#) together with the temperature dependence of the magnitude $\frac{d(M_{FC}-M_{ZFC})}{dT}$ (see inset) which is proportional to the activation energy barrier distributions in the measured temperature range. A narrow energy barrier distribution near 23 K is observed.

Assuming that this maximum represents the blocking temperature distribution of the small α -Fe(Pd) precipitates, $d = 9$ nm in diameter, with a magnetocrystalline energy of about $K_{Ca} \sim 1 \times 10^4$ J m⁻³ [24] the mean blocking temperature T_B may be estimated as $T_B \approx \frac{K_{Ca}d^3}{25k_B} = 21$ K, with k_B the Boltzmann constant. This temperature is close to that estimated from the inset of [Figure 5](#).

In the FC curve, an increase in the magnetic moment below about 80 K is measured, which is observed for different values of applied field (not shown), suggesting a spin glass-like behavior at low temperature. This phenomenon is frequently reported in magnetic nano-objects [25-28], being ascribed to surface effects promoting ‘spin canting’, ‘spin pinning’ or ‘broken exchange bonds’. This effect will be addressed in more detail below.

The hysteresis mechanisms, leading to changes in the array magnetization were further investigated by measuring the hysteresis loops at different temperatures between 5 K and 800 K, for two field configurations: with the applied field parallel (PA) to the NWs axis and with the field perpendicular (PE) to this direction. The results for the PA and PE configurations shown in [Figure 6](#), between 5 K and 800 K, are consistent with a magnetization easy axis close to the NWs axis, as expected because of the array’s shape anisotropy. Both, coercivity and remanence decrease with temperature in PA and PE configurations, as illustrated in [Figure 6c](#) and [Figure 6d](#).

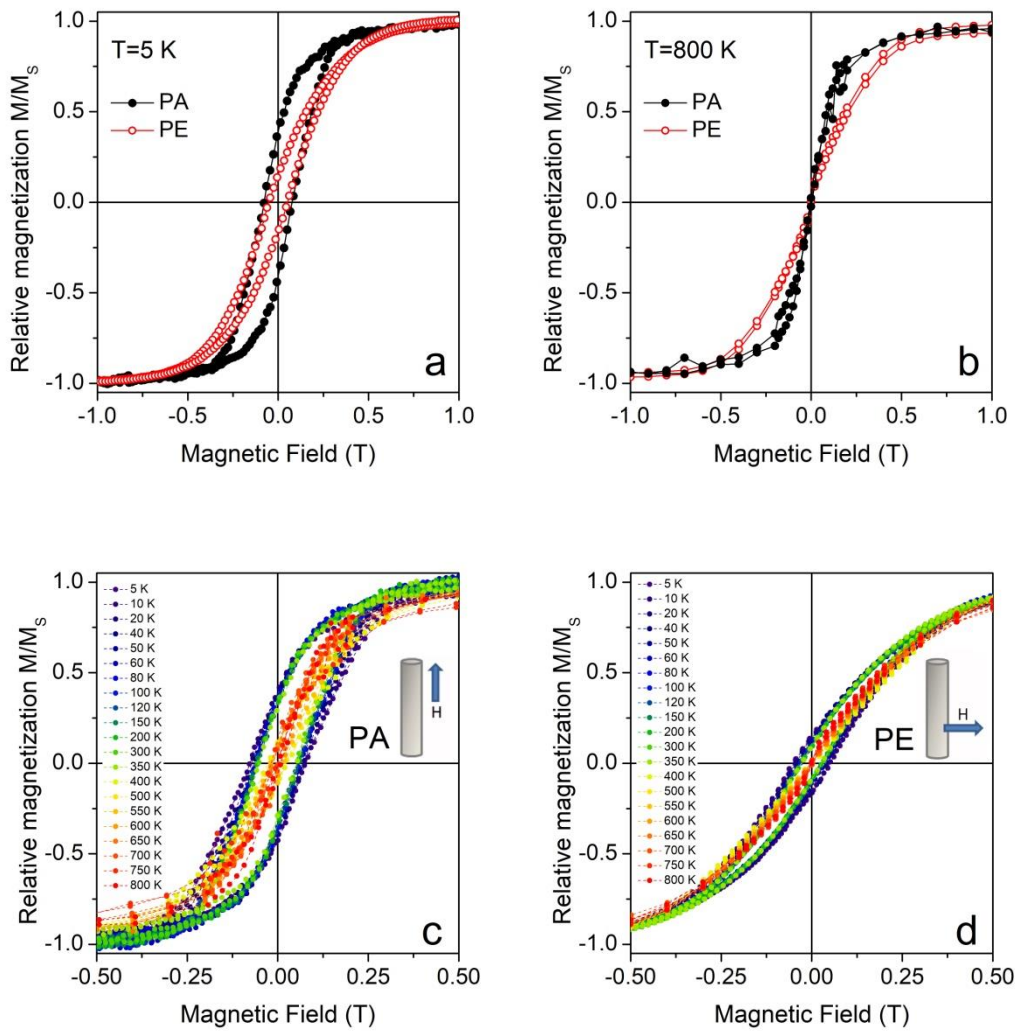


Figure 6. Hysteresis loops measured with the field applied in the PA and PE configurations, at $T=5$ K (a) and at $T=800$ K (b). Hysteresis loops with the field applied in the PA (c) and in the PE (d) configurations, at all the measured temperatures from $T=5$ K to $T=800$ K. All figures show a close-up of the low field region, while the maximum applied field was ± 2 T in every case.

Figure 7 shows the temperature dependence of the coercive field $\mu_0 H_C$, and the relative remanent magnetization (or squareness $S = M_r/M_s$) in the range 5 K to 800 K, where a quite smooth transition between measurements at low and high temperature regimes—taken in different equipments—is observed.

Both magnitudes undergo a similar transition at about 100 K, where two regimes can be clearly identified. The temperature dependence of coercivity below 100 K is well fitted by a linear law $H_c(T) = H_c(0) - \gamma T$, where $H_c(0)$ is the coercivity at $T = 0$ K, and γ is a fitting parameter; in our case, $H_c(0) = (80 \pm 2)$ mT, and $\gamma = (0.32 \pm 0.03)$ mT K⁻¹; the best fit is shown as a solid yellow line in **Figure 7**. At these low temperatures, frozen spin-glass-like surface spins are strongly pinned by exchange interaction with ordered core spins and

hence extra energy is needed to switch the core spins. This “core-shell” interaction in the individual NWs is likely the responsible of the observed increase in coercive field at low temperatures.

Above 100 K, a linear coercivity decrease with temperature is also observed. In this case it is possible to correlate this dependence with a thermally activated, nucleation-controlled magnetization reversal mechanism. Hence, the temperature and field dependence of the activation energy barrier and the coercive field may be described as [29, 30]:

$$E = E_0 \left(1 - \frac{H}{H_0} \right) \quad (1)$$

$$\mu_0 H_C = \mu_0 H_0 - \left[\frac{\mu_0 H_0 25 k_B}{E_0} \right] T. \quad (2)$$

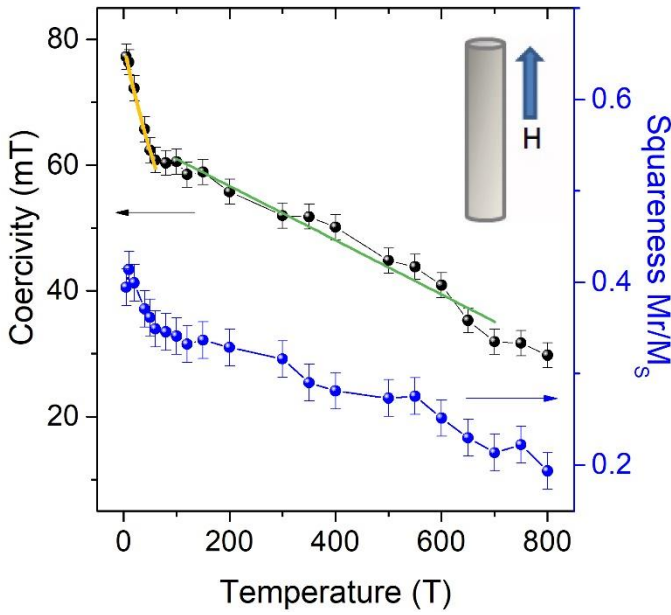


Figure 7. Temperature dependence of the coercive field (left axis) and the relative remanence or squareness ratio S (right axis), taken from the hysteresis loops shown in Figure 6 for the PA field configuration. The yellow and the green solid lines over coercivity data correspond to linear fits described in the text.

Here, parameters $\mu_0 H_0$ and E_0 are respectively, the critical field for magnetization reversal and the activation barrier height at $T=0$ K; the slope of the line described by Eq. (2) is then given by $\frac{\mu_0 H_0 25 k_B}{E_0}$. The fitting of experimental data to Eqs. (1) and (2) lead to activation energy values of (320 ± 20) kJ mol⁻¹ (3.3 ± 0.2 eV) and a critical reversal field at 0 K of (65 ± 1) mT. The activation energy values are comparable to those reported for a mechanism of reverse domain nucleation in Fe nanowires [31] (2.4 - 5.1 eV), and Fe-Rh nanowires [32] (2.1 - 4 eV) and larger by a factor two for Fe-Pd biphasic NWs above 300 K [15] (1.7 eV).

The temperature dependence of saturation magnetization M_s is shown in Figure 8 for the full range between 5 K and 800 K. The two regimes noticed for coercivity and squareness in Figure 7 are also identified in M_s , with an upturn below 100 K —see Figure 8— likely arising from the spin glass-like contribution from magnetic moments in surface/interface zones in the NWs, which can be described by [33]:

$$\frac{M_s(T)}{M_s(0)} = A \exp(-T/T_f), \quad (3)$$

where $M_s(0)$ is the saturation magnetization at 0 K, A is the limit contribution at $T=0$ K and T_f is the freezing temperature, characteristic of the spin-glass transformation.

In addition to this low temperature spin-glass phase contribution to saturation magnetization, another one exists in the whole temperature range, between 5 K and 800 K, arising from the main phase inside the nanowires. This contribution can be well described by the phenomenological expression:

$$\frac{M_s(T)}{M_s(0)} = [1 - (T/T_c)^a]^b, \quad (4)$$

where T_c is the Curie temperature of the NW array, and a and b are fitting parameters. By taking the appropriate limits, this empiric expression can approximate the $M(T)$ complex behavior of the “core spins” at very low temperature, below about $0.4 T_c$, while reproducing a Bloch-like behavior is obtained near the Curie temperature. In fact, in the low temperature limit, $T \rightarrow 0$, $M(T) \propto (1 - cT^a)$ with c a constant, while for the limit $(T_c - T) \rightarrow 0$ Eq. (4) can be written as $M_s(T) \propto (T_c - T)^b$, taking the shape of a critical expression with $b = \frac{1}{\beta}$, being β the critical exponent [34].

Figure 8 shows the relative saturation magnetization $M_s(T)/M_s(5 \text{ K})$ (assuming that $M_s(0) \approx M_s(5 \text{ K})$), together with the curve resulting from the best fit of the sum of Eq. (3) and Eq (4) to experimental data:

$$\frac{M_s(T)}{M_s(0)} = A \exp(-T/T_f) + [1 - (T/T_c)^a]^b. \quad (5)$$

Eq. (5) provides a good description of the data points in the whole temperature range, with the parameters values given in Table 1.

The low-temperature magnetization increase described by Eq. (3) has also been observed in small-sized nanoparticle systems, in the range from 2.5 nm to 25 nm, being explained by considering the quantization of the spin-wave spectrum due to the small finite size of the particles [35, 36], or in different systems by a surface effect [37-39]. In our case, the NWs are ~50 nm in diameter so such strong confinement effects are not expected. On the other hand, a differential contribution arising from the relatively large amount of spins in surface (misaligned) configurations, leading to a non-uniform magnetization through the nanostructures cannot be excluded. It is likely that the wires exhibit a magnetic ordered core, surrounded by a surface shell of disordered spins with a large number of broken exchange bonds, which can result in frustration and spin disorder. These spins are expected to freely fluctuate at

high temperatures, more than those in the core, but they freeze at low temperatures in a disordered “spin-glass like” structure, being the energy barrier for freezing $k_B T_f$ intimately related to the exchange interactions. In the present case, we obtain an energy $k_B T_f = (11 \pm 1) \times 10^{-22}$ J, which is of the same order of magnitude as the exchange coupling constant between first neighbors ($J_{Fe-Fe(fcc)} = 3.52 \times 10^{-22}$ J and $J_{Fe-Pd} = 17.3 \times 10^{-22}$ J [40]) inside the nanomaterial.

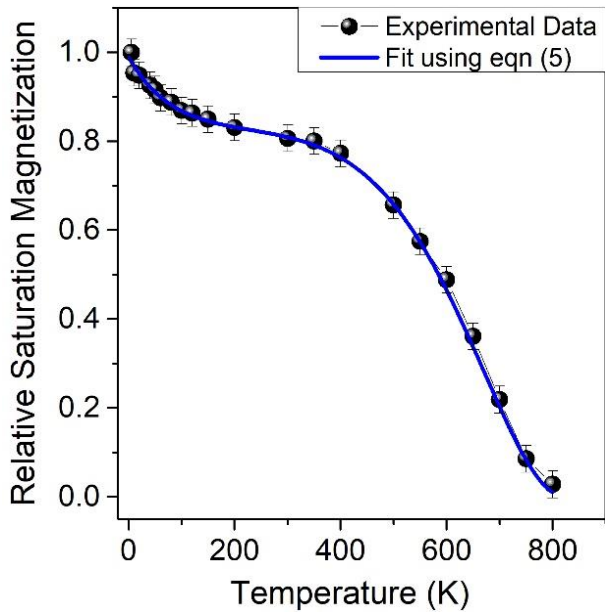


Figure 8. Temperature dependence of the saturation magnetization relative to its value at 5 K. The solid line corresponds to the fitting of Eq. (5) to experimental data.

Table 1. Fitting parameters of Eq. (5) to $M_S(T)/M_S(5\text{ K})$ experimental data.

Fe85	
A	0.17 ± 0.05
T_f [K]	80 ± 2
T_c [K]	830 ± 20
a	4.8 ± 0.4
$\beta (= b^{-1})$	0.42 ± 0.05

The resulting value of parameter $a = 4.8$ is three times larger than that of the Bloch law in bulk ferromagnets (3/2), indicating that in the present conditions some hypotheses might not be valid. Recently, based on experimental results, an extension of Bloch law has been proposed [41, 42], which also considers a temperature power law but with the exponent dependent on three fundamental conditions: dimensionality, predominant spin and anisotropy. Köbler *et al.* [43] find that for integer spin 3-D exchange interactions, the $T^{9/2}$ power function holds, which agrees with our result.

Concerning the critical exponent $\beta = 0.42 \pm 0.05$ ($= b^{-1}$) resulting from fitting the data in Figure 8, it is close to that obtained with the Monte Carlo method, $\beta = 0.5$ [44], and practically indistinguishable from the value $\beta = 0.44$ reported for FePd₃ [45]. Note that a quite reasonable critical exponent $\beta = 0.42 \pm 0.05$ is derived from the whole temperature range fitting to Eq. (5).

3.3. Effective Anisotropy constant K_{eff}

The temperature dependence of the effective uniaxial anisotropy constant was estimated from the hysteresis loops shown in Figure 6, by applying the area method [46]. This method is based on the magnetization work or amount of energy required to magnetize to saturation in a given direction. Then, the effective anisotropy K_{eff} for each array is related to the area enclosed by the upper branches of the PA and PE hysteresis loops. From Figure 6 we can deduce that the magnetization easy axis for K_{eff} is along the NWs axis (PA) in the whole temperature range. The temperature dependence of K_{eff} for the array is depicted in Figure 9.

Since the magnetocrystalline anisotropy of the major phase in the NWs is quite low ($\sim 2 \times 10^4$ J m⁻³ [25]) then, only contributions arising from magnetostatic energy—the shape anisotropy K_S of a single NW and the magnetostatic anisotropy K_I , associated with inter-wire magnetostatic interaction in the array—are considered. Then, in this simple scenario we have:

$$K_{eff} = K_S + K_I. \quad (6)$$

The total magnetostatic effective anisotropy constant (the one arising from the shape anisotropy of individual nanowires added to that arising from dipolar inter-wire interactions) may be estimated as proposed by Carignan *et al.* [47], so the effective constant can be written as:

$$K_{eff}(T) = \frac{\mu_0 M_S^2(T)}{4} (1 - 3P), \quad (7)$$

where the template’s porosity in the present case is $P = 0.20$.

In order to determine K_{eff} , the value $M_s(0) = (1300 \pm 100)$ kA/m [48, 49] was considered for the $\text{Fe}_{85}\text{Pd}_{15}$ alloy.

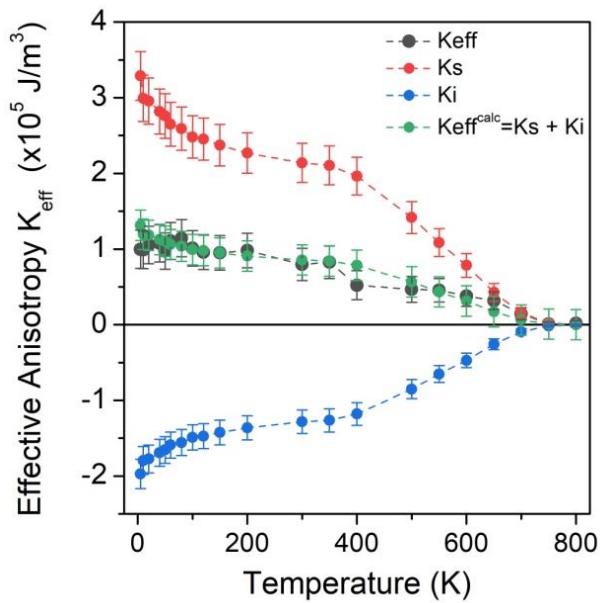


Figure 9. Temperature dependence of the effective magnetic anisotropy K_{eff} in the Fe_{85} NW array between 5 K and 800 K. Contributions to this total effective anisotropy arising from the shape of individual wires, K_s , and from magnetostatic inter-wire interactions K_i are also plotted.

In **Figure 9**, the temperature dependence of K_s and K_i are shown; their respective positive and negative values in the whole temperature range correspond to the field configuration parallel to the NW magnetization easy axis. That is, for the present geometrical values of the NWs length and diameter and the inter-wire distance, the shape anisotropy of the individual cylindrical nanowires is stronger than that arising from the magnetostatic interactions' energy among NWs. Thus, the effective anisotropy estimated by only considering magnetostatic contributions describes quite well the experimental data particularly above 100 K, supporting the dependence on M_s^2 proposed.

In the range 5 K - 100 K, even when experimental data are statistically indistinguishable from the calculated values, errors are too large and other effects cannot be excluded. As commented before, the observed temperature dependence of the coercive field, the relative remanence and the saturation magnetization are consistent with a spin glass-like behavior associated with surface spin configurations.

4. Conclusion

The main phase in $\text{Fe}_{85}\text{Pd}_{15}$ as-deposited nanowires is the metastable $\gamma\text{-Fe(Pd)}$ *fcc* A1 disordered solid solution, with mean grain size of (15 ± 5) nm. A quite small volume fraction ($\sim 3\%$) of about 9 nm grains of the *bcc* $\alpha\text{-Fe(Pd)}$ solid solution is also detected.

After a heating-cooling thermal cycle between 350 K and 1000 K, the $\gamma\text{-Fe(Pd)}$ *fcc* metastable phase still predominates (97 %). The corresponding diffraction maxima are shifted to higher angles, indicating a slight contraction in the lattice parameter, likely due to the annealing of atomic defects and the debut of structural ordering at high temperature.

The saturation magnetization curve between 5 K and 800 K is well described by the superposition of two contributions: one arising from surface spins behaving as a “shell magnetic phase” in the NWs and a second one, a “core magnetic phase”, involving the magnetic moments inside the wires. The core contribution is accurately described by a phenomenological expression, which reproduces a Bloch-like law as $T \rightarrow 0$, with an exponent larger than $3/2$, and near the Curie temperature a critical exponent $\beta = 0.42 \pm 0.05$ could be estimated. On the other hand, the spin-glass-like phase contribution becomes detectable below 100 K, being the freezing temperature $T_f = (80 \pm 2)$ K, and the energy $k_B T_f$ comparable to the exchange interactions in FePd systems. These regimes (below and above 100 K) are also observed in the coercivity and the relative remanence curves as functions of temperature.

The temperature dependence of the coercive field in the array between 100 K and 800 K is consistent with a mechanism involving the nucleation of reverse domains and the subsequent propagation of the domain walls, with an activation energy of (320 ± 20) kJ mol⁻¹ (3.3 ± 0.2 eV) and a critical field for magnetization reversal of (65 ± 1) mT, at 0 K.

The effective magnetic anisotropy estimated from the hysteresis loops between 5 K and 800 K shows a good concordance with an effective anisotropy arising only from magnetostatic effects, that is the shape anisotropy of individual NWs and dipolar inter-wire interaction in the array.

CRedit authorship contribution statement

Paula G. Bercoff: Conceptualization, Methodology, Validation, Formal analysis, Resources, Supervision, Visualization, Project administration, Funding acquisition, Writing – original draft, review & editing.

Soledad Aprea: Investigation, Formal analysis, Visualization.

Eva Céspedes: Methodology, Validation, Investigation, Formal analysis, Writing – review & editing.

Silvia E. Urreta: Conceptualization, Methodology, Formal analysis, Visualization, Writing – original draft, review & editing.

José Luis Martínez: Validation, Investigation, Supervision, Resources, Writing – review & editing, Funding acquisition.

Manuel Vázquez: Resources, Writing – review & editing, Funding acquisition.

All authors read and approved the final manuscript.

Data availability

The data supporting this article have been included as part of the Supplementary Information.

Conflicts of Interest

There are no conflicts of interest to declare

Acknowledgements

The authors are greatly indebted to Dr. Alberto Caneiro, from the Argentinian Enterprise Y-TEC (YPF Tecnología S.A.- YPF-CONICET), and to Dr. Neven Biskup from the Departamento de Física de Materiales, Universidad Complutense de Madrid, who performed different TEM-HRTEM measurements. P.G.B. thanks Bruno Castellano for his assistance in writing the Python code used for the fittings. This work has been partially funded by Secyt-UNC, ANPCyT-FONCyT and Conicet (Argentina). We also acknowledge the financial support of the Spanish Ministry of Science and Innovation (project MCIN/AEI/10.13039/501100011033) to the projects PID2021-122477OBI00, PID2021-129254B-C21, TED2021-129254B-C22 and PID2022-137567NB-C21.

References

- [1] M. Matsui, T. Shimizu, H. Yamada, K. Adachi. Magnetic properties and thermal expansion of Fe-Pd invar alloys, *J. Magn. Mater.* 15–18 (1980) 1201.
- [2] T. Nakayama, M. Kikuchi, K. Fukamichi. Young's modulus and the Delta E effect of Fe-Pd Invar alloys, *J. Phys. F* 10 (4) (1980) 715.
- [3] M. Matsui, T. Shimizu, K. Adachi. Invar anomalies of Fe-Pd alloys, *Physica B+C* 119 (1983) 84.
- [4] M. Matsui, K. Adachi. Magnetostriction of Fe-Pd Invar, *J. Magn. Mater.* 31–34 (1983) 115.
- [5] V. Gehanno, A. Marty, B. Gilles, Y. Samson. Magnetic domains in epitaxial ordered FePd(001) thin films with perpendicular magnetic anisotropy, *Phys. Rev. B* 55 (1997) 12552.
- [6] V. Sánchez-Alarcos, V. Recarte, J. I. Pérez-Landazabal, C. Gómez-Polo, V. A. Chernenko, M. A. González. Reversible and irreversible martensitic transformations in Fe-Pd and Fe-Pd-Co alloys, *Eur. Phys. J. Special Topics* 158 (2008) 107–112.
- [7] R. D. James, M. Wuttig. Magnetostriction of martensite, *Philos. Mag. A* 77 (1998) 1273.
- [8] R. C. O'Handley. Model for strain and magnetization in magnetic shape-memory alloys. *J. Appl. Phys.* 83, 6 (1998) 3263-3270.
- [9] K. Ullakko, J. K. Huang, C. Kantner, R. C. O'Handley, V. V. Kokorin. Large Magnetic-Field-Induced Strains in Ni₂MnGa Single Crystals. *Appl. Phys. Lett.* 69, 13 (1996) 1966-1968.
- [10] J. Cui, T. W. Shield, R. D. James. Phase transformation and magnetic anisotropy of an iron–palladium ferromagnetic shape-memory alloy, *Acta Mater.* 52 (2004) 35.
- [11] Y. Ma, M. Zink, S. G. Mayr. Biocompatibility of single crystalline Fe₇₀Pd₃₀ ferromagnetic shape memory films, *Appl. Phys. Lett.* 96 (2010) 213703.
- [12] G. Barrera, F. Celegato, M. Cialone, M. Coisson, P. Rizzi, P. Tiberto. Effect of the Substrate Crystallinity on Morphological and Magnetic Properties of Fe₇₀Pd₃₀ Nanoparticles Obtained by the Solid-State Dewetting. *Sensors* 21 (2021) 7420. DOI: 10.3390/s21217420
- [13] M. S. Viqueira, S. E. García, S. E. Urreta, G. Pozo-López, L. M. Fabietti. Hysteresis properties of hexagonal arrays of FePd nanowires, *IEEE Trans. on Magnetism* 49 (8) (2013) 4498-4501. DOI: 10.1109/TMAG.2013.2258461.
- [14] M. S. Aprea, J. S. Riva, P. G. Bercoff, M. Vázquez. Temperature dependence of magnetic anisotropy in a cylindrical Fe₆₅Pd₃₅ nanowire array. *Journal of Magnetism and Magnetic Materials* 564, 2 (2022) 170166. DOI: 10.1016/j.jmmm.2022.170166.
- [15] P. G. Bercoff, E. Céspedes, S. Aprea, S. E. Urreta, J. L. Martínez, M. Vázquez. High temperature magnetic and structural transformations in Fe-Pd nanowires. *Materials Research Bulletin* 169 (2024) 112540. DOI: 10.1016/j.materresbull.2023.112540.
- [16] A. Zarzycki, M. Perzanowski, M. Krupinski, M. Marszalek. Solid-State Dewetting as a Driving Force for Structural Transformation and Magnetization Reversal Mechanism in FePd Thin Films, *Materials* 16 (2023) 92. DOI: 10.3390/ma16010092.
- [17] S. Bahamida, A. Fnidiki, M. Coisson, E. S. Olivetti, G. Barrera, F. Celegato, P. Tiberto, M. Boudissa.

Disordered to ordered phase transformation: Correlation between microstructure and magnetic properties in Fe–Pd thin films. *J. Appl. Phys.* 131 (2022) 123902; DOI: 10.1063/5.0085898.

[18] T. B. Massalsky, *Binary Alloys Phase Diagrams*, ASM International Materials Park, Ohio, 1986. 113–126. DOI: 10.1016/j.pnsc.2013.02.001

[19] H. Yabe, T. Kuji. Crystal structure of iron-palladium alloys by mechanical alloying, *J. Metastable Nanocryst. Mater.* 24-25 (2005) 439-442.

[20] H. Yabe, R. C. O’Handley, T. Kuji. Magnetic properties of metastable Fe–Pd alloys by mechanical alloying, *J. Magn. Magn. Mater.* 310, 2 (2007) 2500-2502.

[21] H. Masuda, K. S. Fakuda. Ordered metal nanohole arrays made by a two-step replication of honeycomb structures of anodic alumina, *Science* 268 (1995) 1466-1468.

[22] K. Nielsch, J. Choi, K. Schwirn, R.B. Wehrspohn, U. Gosele. Self-ordering regimes of porous alumina: the 10% porosity rule, *Nano Lett.* 2 (2002) 677-680.

[23] T. Liu, L. Ma, S. Q. Zhao, D. D. Ma, L. Li, G. Cheng, G. H. Rao. Crystal structure and magnetic properties of Fe_xPd_{1-x} thin films annealed at 550 °C. *J Mater Sci: Mater Electron.* 28 (2017) 3616–3620. DOI: 10.1007/s10854-016-5963-6.

[24] N. I. Vlasova, N. N. Shchegoleva, A. G. Popov, G. S. Kandaurova. Ferroelastic Domains and Phases in Ferromagnetic Nanostructured FePd Alloy, *Fizika Metallov i Metallovedenie*, Vol. 110, No. 5 (2010) 470–485.

[25] D. J. Zhang, K. J. Klabunde, C. M. Sorensen, G. C. Hadjipanayis. Magnetization temperature dependence in iron nanoparticles, *Phys. Rev. B* 58 (1998) 14167.

[26] M. Zheng, L. Menon, H. Zeng, Y. Liu, S. Bandyopadhyay, R.D. Kirby, D.J. Sellmyer. Magnetic properties of Ni nanowires in self-assembled arrays, *Phys. Rev. B* 62 (2000) 12282.

[27] M. Z. Wu, Y. D. Zhang, S. Hui, T. D. Xiao, S. H. Ge, W. A. Hines, J. I. Budnick. Temperature dependence of magnetic properties of SiO₂-coated Co nanoparticles, *J. Magn. Magn. Mater.* 268 (2004) 20.

[28] K. Mandal, S. Mitra, P.A. Kumar. Deviation from Bloch T^{3/2} law in ferrite nanoparticles, *Europhys. Lett.* 75 (2006) 618.

[29] S. Chikazumi. Mechanism of high coercivity in rare-earth permanent magnets, *J. Magn. Magn. Mater.* 54-57 (1986) 1551-1555.

[30] P. Gaunt. Magnetic viscosity and thermal activation energy, *J. Appl. Phys.* 59 (1986) 4129-4132. DOI: 10.1063/1.336671.

[31] P. M. Paulus, F. Luis, M. Kröll, G. Schmid, L. J. de Jongh. Low-temperature study of the magnetization reversal and magnetic anisotropy of Fe, Ni, and Co nanowires, *J. Magn. Magn. Mater.* 224 (2001) 180-196.

[32] J. S. Riva, G. Pozo-López, A. M. Condó, L. M. Fabietti, S. E. Urreta. Low temperature ferromagnetism in Rh-rich Fe-Rh granular nanowires, *J. All. Comp.* 747 (2018) 1008-1017.

[33] R. Aquino, J. Depeyrot, M. Sousa, F. A. Tourinho, E. Dubois, R. Perzynski. Magnetization temperature dependence and freezing of surface spins in magnetic fluids based on ferrite nanoparticles, *Phys. Rev. B* 72 (2005)184435.

[34] J. Mira, J. Rivas, M. Vázquez, J. M. García-Beneytez, J. Arcas, R. D. Sánchez, M. A. Señarís-Rodríguez. Critical exponents of the ferromagnetic-paramagnetic phase transition of La_{12x}Sr_xCoO₃ (0.20<x<0.30), *Phys. Rev. B* 59 (1) (1999) 123-126.

[35] K. Mandal, S.Mitra, P. A. Kumar, S. Mørup. Deviation from the Bloch T^{3/2} law in ferrite nanoparticles, *Europhys. Lett.* 75 (2006) 618.

[36] S. Mørup. Comment on “Deviation from the Bloch T^{3/2} law in ferrite nanoparticles” by K. Mandal et al. *Europhysics Letters* (2007) 77. DOI: 10.1209/0295-5075/77/27003.

[37] R. H. Kodama and A. E. Berkowitz, E. J. McNiff, Jr., S. Foner. Surface Spin Disorder in NiFe₂O₄ Nanoparticles, *Phys. Rev. Lett.* 77 (2) (1996) 394-397;

[38] K. Chakrabarti, B. Sarkar, V. Dev Ashok, K. Das, S. S. Chaudhuri, S. K. De. Interfacial magnetism and exchange coupling in BiFeO₃–CuO nanocomposite, *Nanotechnology* 24 (2013) 5057112- 21;

[39] K. Maaz, A. Mumtaz, S. K. Hasanain, M. F. Bertino, Temperature dependent coercivity and magnetization of nickel ferrite nanoparticles, *J. Magn. Magn. Mater.* 322 (2010) 2199–2202

[40] Lisha Wang, Zhaohui Fan, A. G. Roy, D. E. Laughlin. Effects of atomic ordering on the Curie temperature of FePd L10 type alloys, *J. Appl. Phys.* 95 (11) (2004) 7483-7485.

[41] U. Köbler, A. Hoser. Magnetism of powder samples and of single crystals, *J. Magn. Magn Mater.* 349 (2014) 88.

[42] U. Köbler, A. Hoser, W. Schafer. On the temperature dependence of the magnetic excitations, *Phys. B* 364 (2005) 55.

[43] U. Köbler, A. Hoser. Stable magnetic universality classes for T→0, *Phys. B* 362 (2005) 295–305.

[44] L Rohman, E Supriyanto, K Sa’diyah, D Djuhana. Curie temperatures and critical exponent properties of FePd ferromagnetic materials by data simulations

approach, *Journal of Physics: Conf. Series* 1170 (2019) 012018. DOI:10.1088/1742-6596/1170/1/012018.

[45] M. Seeger, H. Kronmüller. Phase transition in ordered and disordered ferromagnets, *J. Magn. Magn Mater.* 78 (1989) 393-402

[46] B. D. Cullity, C. D. Graham. *Introduction to Magnetic Materials*, Second Edition. Wiley-IEEE Press, March 2010.

[47] P. Carignan, C. Lacroix, and A. Ouimet, M. Ciureanu, A. Yelon, D. Ménard. Magnetic anisotropy in arrays of Ni, CoFeB, and Ni/Cu nanowire, *J. Appl. Phys.* 102, 2 (2007) 023905.

[48] H. Yabe, R. C. O'Handley, T. Kuji. Magnetic properties of metastable Fe–Pd alloys by mechanical alloying, *J. Magn. Magn Mater.* 310 (2007) 2500–2502

[49] S. C. Hernández, B. Y. Yoo, E. Stefanescu, S. Khizroev, N. V. Myung. Electrodeposition of iron–palladium thin films, *Electrochimica Acta* 53 (2008) 5621–5627.